gated via nucleation of dimers at 40 K and subsequent annealing to 110 K and 150 K respectively. The homogeneous spatial distribution and the narrow range of sizes are obvious in both STM images.

The diffusion barrier of the pre-nucleated dimers is twice as high as that of Ag adatoms[10] and the dimers are stable over an extended temperature range (Fig. 2). On annealing the surface to temperatures >100 K, dimer diffusion and/or dissociation and subsequent adatom diffusion sets in, resulting in the formation of larger clusters by coalesence. The size of these clusters depends exponentially on the annealing temperature.

Diffusion-controlled aggregation can also be used to synthesize one-dimensional aggregates. One-dimensional systems have, indeed, been the focus of much interest because of their unique behaviour and the fact that certain problems can be solved exactly for these systems[11]. The growth of one-dimensional aggregates makes use of the directional anisotropy of Λ_a (ref. 12). For surfaces with C_{2v} symmetry, there are two different migration barriers, representing two orthogonal directions. An example is the diffusion of Cu atoms on the Pd (110) surface, where the migration barriers are 0.76 and 0.51 eV for the orthogonal [001] and [1$\bar{1}$0] directions, respectively[13]. The value of Λ_a [1$\bar{1}$0] is thus larger than Λ_a [100] giving rise to a faster growth rate along the [1$\bar{1}$0] channels. With decreasing deposition temperature, the ratio of the rate of diffusion along the close-packed direction to that in the perpendicular direction increases. It should therefore be possible to freeze out cross-channel diffusion along [100] while diffusion along the [1$\bar{1}$0] channels is still sufficiently fast. Under such favourable conditions, exclusively one-dimensional chains of adatoms should grow along the [1$\bar{1}$0] direction of the surface.

The experimental realization of such a situation is shown in Fig. 3*b*, in which Cu aggregates are grown and imaged on the Pd (110) surface at 300 K. At this temperature, the jump rate in the easy [1$\bar{1}$0] direction is 10^4 times higher than that across the channel walls (assuming approximately equal prefactors[14]) and we observe the aggregation of long monatomic Cu chains with lengths up to several hundred Å. The average length of these one-dimensional Cu wires can be tailored, for example by varying the deposition temperature. Because diffusion along [100] is already negligible at 300 K, nucleation at temperatures <300 K will also result in the aggregation of one-dimensional chains, the average length of which will decrease with decreasing temperature (that is, decreasing Λ_a[1$\bar{1}$0]). Whereas at 300 K for a total coverage of 0.05 ML the monatomic Cu chains consist of an averge of 130 Cu atoms, at 180 K (at the same coverage) the average chain is composed of only 10 Cu atoms.

The monatomic Cu chains aggregated on the Pd (110) surface are metastable nanostructures. Upon a short anneal to, or direct growth at, 350 K, two-dimensional lens-shaped islands, several atomic rows wide, are formed. This is demonstrated in Fig. 3*c*, which shows the structure produced by growth at 350 K: two-dimensional Cu islands with an average aspect ratio of 15 are formed. The metastable character of the long one-dimensional Cu chains is not surprising. Field ion microscopy measurements[15–17] and molecular dynamics calculations[18] have revealed that in general the linear one-dimensional clusters constitute the equilibrium structure only at small sizes ($n < 10$). For Cu on Pd (110), however, recent molecular dynamics simulations[19] reveal that at 0 K one-dimensional chains (which can be very long) are the energetically preferred structures. It appears to be the entropy gain associated with the transition from one to two dimensions that drives the Cu aggregates on Pd (110) to two-dimensional structures at elevated temperatures[13].

This approach of diffusion-controlled aggregation for the synthesis of one- and two-dimensional matter is not restricted to the systems discussed, nor to metal aggregates on metal surfaces. Diffusion-controlled aggregation is applicable for all growth systems in the kinetic regime (including metals on semiconductors or insulators), and one should always be able to find a temperature window in which one- or two-dimensional aggregates (substrates with directionally anisotropic diffusion) can be produced by manipulating Λ_a and Λ_1. □

Received 29 July; accepted 22 September 1993.

1. Eigler, D. M. & Schweizer, E. K. *Nature* **344,** 524–526 (1990).
2. Kern, R. in *Interfacial Aspects of Phase Transitions* (ed. Mutaftschiev, B.) 287–312 (Reidel, Dordrecht, 1982).
3. Witten, T. A. & Sander, L. M. *Phys. Rev.* B**27,** 5686–5697 (1983).
4. Hwang, R. Q., Schröder, J., Günther, C. & Behm, R. J. *Phys. Rev. Lett.* **67,** 3279–3282 (1991).
5. Roeder, H., Brune, H., Bucher, J. P. & Kern, K. *Surf. Sci.* (in the press).
6. Venables, J. A., Spiller, G. D. T. & Hanbücken, M. *Rep. Prog. Phys.* **47,** 399–459 (1984).
7. Ayrault, G. & Ehrlich, G. *J. Chem. Phys.* **60,** 281–294 (1974).
8. Michely, Th. & Comsa, G. *Surf. Sci.* **256,** 217–226 (1991).
9. Jena, P., Khanna, S. N., Rao, B. K. (eds) *Physics and Chemistry of Finite Systems: From Clusters to Crystals* (Kluwer, Dordrecht, 1992).
10. Massobrio, C. & Blandin, Ph. *Phys. Rev.* B**47,** 13687–13694 (1993).
11. Solyom, J. *Adv. Phys.* **28,** 201–303 (1979).
12. Bonzel, H. in *Diffusion in Metals and Alloys* (ed. Mehrer, H.) Ch. 13 (Springer, Berlin, 1992).
13. Bucher, J. P., Hahn, E., Fernandez, P., Massobrio, C. & Kern, K. *Phys. Rev. Lett.* (submitted).
14. Tsong, T. T., Liu, J. & Wu, C. W. in *Physics and Chemistry of Finite Systems: From Clusters, to Crystals* (eds Jena, P *et al.*) 1039–1045 (Kluwer, Dordrecht, 1992).
15. Basset, D. W. *Thin Solid Films* **48,** 237–249 (1978).
16. Fink, H. W. & Ehrlich, G. *Surf. Sci.* **110,** L611–L614 (1981).
17. Schwoebel, P. R. & Kellog, G. L. *Phys. Rev. Lett.* **61,** 578–581 (1988).
18. Wright, A. F., Daw, M. S. & Fong, C. Y. *Phys. Rev.* B**42,** 9409–9419 (1990).
19. Fernandez, P. & Massobrio, C. *Surf. Sci.* (submitted).

ACKNOWLEDGEMENTS. This research is supported by the Schweizerischer Nationalfonds, the Deutsche Forschungsgemeinschaft and the Forschungszentrum Jülich.

Atomic-resolution chemical analysis using a scanning transmission electron microscope

N. D. Browning, M. F. Chisholm & S. J. Pennycook

Solid State Division, Oak Ridge National Laboratory, PO Box 2008, Oak Ridge, Tennessee 37831-6030, USA

THE high angle elastic scattering of electrons in scanning transmission electron microscopy depends strongly on the atomic number Z, of the sample atoms, through the Z^2 dependence of the Rutherford scattering cross-section[1]. The detection of scattered electrons at high angles and over a large angular range (75–150 milliradians) removes the coherent effects of diffraction, and the resulting incoherent image provides a compositional map of the sample with high atomic-number contrast[1]. If a fine electron probe is used, and the sample is a crystalline material oriented along one of its principal axes, individual columns of atoms can be imaged in this way[2]. Electrons scattered at low angles are not used in this detection scheme, and are thus available for simultaneous electron energy-loss spectroscopy[3]; in principle, this combination of techniques should allow the direct chemical analysis of single atomic columns in crystalline materials. Here we present electron energy-loss spectra from expitaxial interfaces between cobalt silicide and silicon, which confirm that atomic resolution can be achieved by this approach. The ability to correlate structure and chemistry with atomic resolution holds great promise for the detailed study of defects and interfaces.

The basis of obtaining electron energy-loss spectra (EELS) with atomic resolution is the high-resolution Z-contrast imaging technique in the scanning transmission electron microscope (STEM) (Fig. 1). Using the high-angle annular dark-field detector makes thermal diffuse scattering the dominant contribution to the detected intensity and allows us to consider each atom as scattering independently with a cross-section that approaches the Z^2 dependence on atomic number. For thin specimens, where there is no dynamical diffraction, the detected intensity will

therefore consist of a convolution of the probe profile and an object function which is strongly peaked at the atom sites. As the width of the object function is typically ~0.1 Å, this means that the spatial resolution is limited only by the 2.2-Å probe size of the STEM (VG Microscopes HB501 UX). In zone-axis orientations where the probe size is smaller than the atomic spacing, the individual atomic columns can therefore be excited individually and an atomic resolution compositional map of the specimen is generated. Experimental results show that this high resolution also holds for thicker specimens where dynamical diffraction would be expected to significantly broaden the probe[2]. This is due to the local nature of the high-angle scattering events resulting in a preferential scattering from *s*-type Bloch states. Dynamical diffraction then manifests itself simply as a columnar chanelling effect which scales the scattering cross-section according to thickness[2,4,5]. Differences in intensity due to channelling effects are always less than those due to compositional changes, so the intuitive interpretability of the incoherent image is retained, making it an ideal map with which to position the probe for energy-loss spectroscopy with atomic precision.

As the energy-loss spectrum can be obtained simultaneously with the image (Fig. 1), the probe can be positioned over a single atomic column seen in the image. For an incoherent, large *energy-loss* scattering event that is also generated close to an atomic core, the *s*-type Bloch states will again be preferentially selected, the probe channelling effect will occur, and a similar description of the resolution in terms of a sharp object function convoluted with the probe intensity profile can be applied. Inelastic signals of this nature would be expected to have the same properties as the *Z*-contrast image, that is probe channelling will elminate beam broadening for thicker specimens, allowing the chemical analysis of an individual atomic column within a crystal[6,7]. To avoid dynamical effects on the outgoing inelastically scattered electrons it is necessary to average over a wide angular range. Under these circumstances, the simple classical description of the impact parameter[8] approximates well to the full quantum-mechanical results[9–11], and Fig. 2 shows the expected spatial resolution of the energy-loss signal.

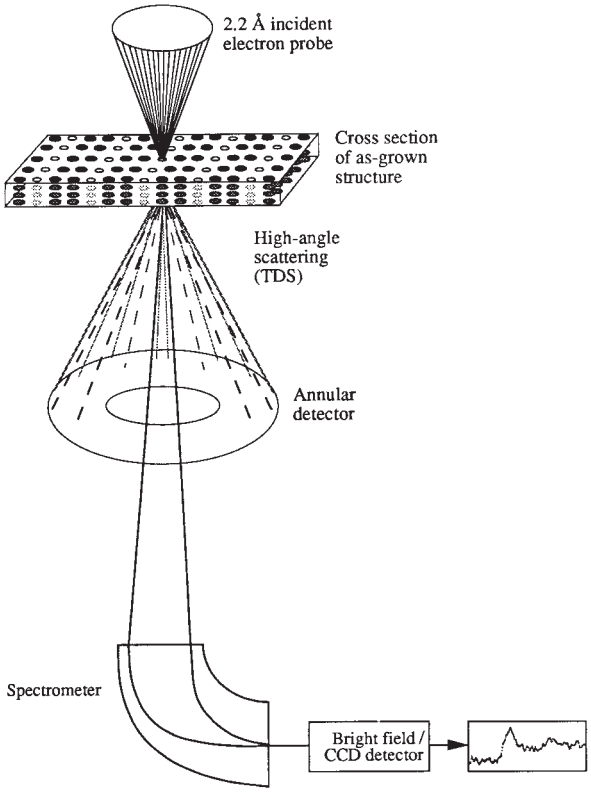

FIG. 1 Schematic diagram of the STEM detectors showing the high-angle scattering used for *Z*-contrast imaging. Collecting at high angles reduces coherence only to correlations between nearest neighbours of atoms in the same column[5], and the large angular range of the detector averages any coherent scattering of the outgoing electrons. For thin crystalline materials in major zone-axis orientations, where the probe is smaller than the atomic column separation, a map of the location of the atomic columns can be generated where the intensity is directly dependent on columnar composition.

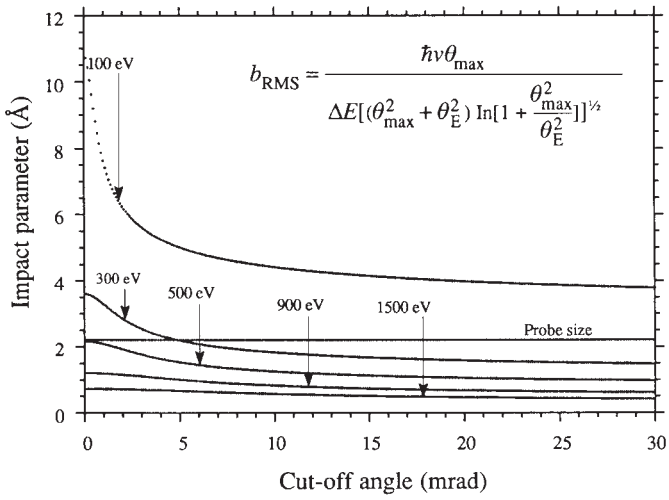

FIG. 2 The range of the inelastic scattering event as a function of the spectrometer collection angle for various energy losses can be estimated from the root mean square impact parameter, b_{RMS} (v is the electron velocity, θ_{max} is the collection angle defined by the aperture size, ΔE is the energy loss and θ_E is the characteristic angle given by $\Delta E/2E_0$, where E_0 is the incident beam energy). Using the maximum collection angle allowed by the inner angle of the dark field detector (30 mrad), for core-losses above 300 eV the impact parameter becomes smaller than the probe, allowing atomic resolution to be obtained[6,7]. Note that this is a classical free space calculation; dielectric screening may reduce the impact parameter and allow atomic resolution at lower energy losses[16].

This anticipated high spatial resolution is demonstrated by studying epitaxial $CoSi_2$–Si interfaces produced by high-dose implantion of Co^+ ions in a heated Si (001) substrate. Annealing results in a continuous buried $CoSi_2$ layer consisting of {001} terraces separated by occasional {111} facets. Cross-sectional samples, that is with the interface parallel to the beam direction, were prepared for electron microscopy by mechanical polishing and ion-milling. The *Z*-contrast image of a {111} facet is shown in Fig. 3*a*, with the brighter region corresponding to the increased scattering power of the heavier cobalt atoms in the silicide. (Note that the silicon atoms in the silicide are unresolved, producing a uniform bright background of similar intensity to that of the silicon columns in the substrate.) The stacking fault visible at the interface means that the separation of the planes across the boundary corresponds to 2.7 Å rather than the 3.1-Å planar spacing of the bulk.

The demagnification required to obtain the 2.2-Å probe used in these experiments reduces the beam current by a factor of 20–30 over conventional STEM conditions. The current density may, however, still be sufficient to cause significant beam damage to the interface. To reduce the dose on any single atomic column, spectra were obtained while the probe was scanned along planes parallel to the interface using an oscilloscope linescan to maintain its position. (The *Z*-contrast image of the interface was used to select a region where the interface was abrupt for the full width of the scan, indicating no change in spectral intensity moving along the interface would be expected.) To reduce the effects of specimen drift (~2–3 Å min^{-1}) exposure times for the

cobalt $L_{2,3}$ edge were limited to only 5 s (Fig. 3*b*). Figure 3*b* shows that using the large aperture to obtain a high degree of localization reduces the energy resolution of the spectra, with the width of the L_3 edge being ~5 eV. This resolution, however, is quite sufficient to be able to measure relative changes in intensity across the interface. Two reference spectra were obtained from several planes away from the interface, one in the silicon for background subtraction, and the other in the silicide

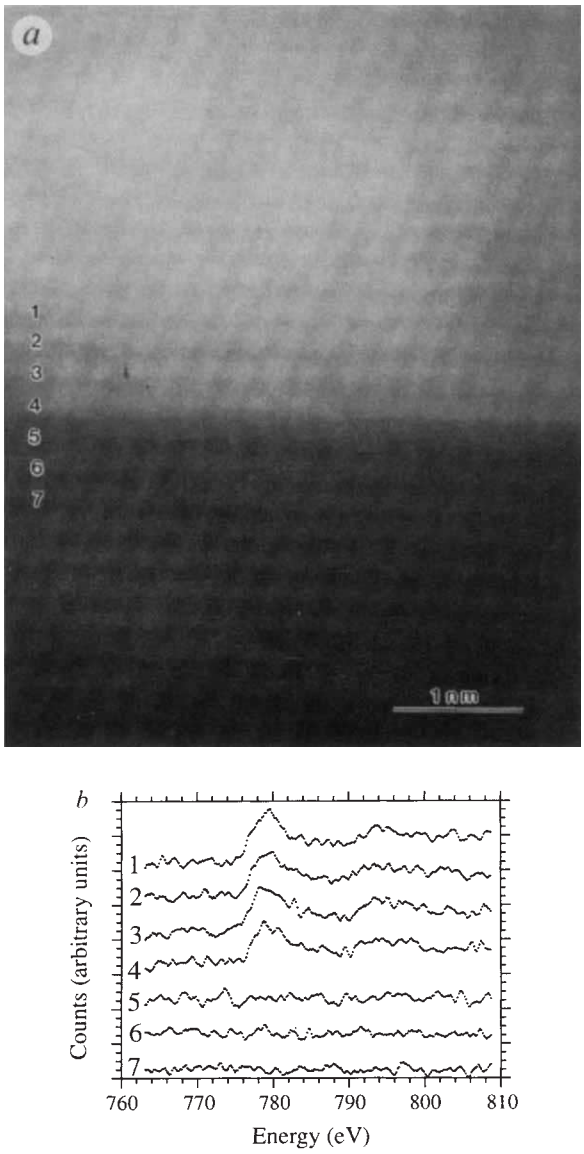

FIG. 3 *a*, *Z*-contrast image of a {111} facet in a $CoSi_2$–Si interface, showing the presence of a stacking fault in the silicon which means that the microscopic orientation of the interface is the twinned 'B'-type. Note that phase contrast simulations of such interfaces have not considered a stacking fault[17] resulting in the erroneous interpretation of interfacial cobalt co-ordination[18]. *b*, Background-stripped cobalt $L_{2,3}$ spectra obtained plane-by-plane across the interface. The background was subtracted by taking multiple spectra at the same energy loss and exposure time from regions of pure silicon of similar thickness, which were summed to improve statistics. This was then scaled to the background of each spectrum from the interface region. Although the intensity of the background is slightly reduced in the silicide the shape is identical, allowing an accurate subtraction of the background which at the same time removes any variations in detector efficiency. The CCD (charge-coupled device) detector used[6,7] here has very low thermal and output noise, so that the noise of the spectra is due only to shot noise in the spectrum itself (~10%).

to obtain an accurate measurement of cobalt L-edge intensity. This procedure assumes that the shapes of the spectra are not affected by multiple scattering, an assumption that is borne out by the constancy of the observed $L_3:L_2$ ratio (Fig. 4*a*). The cobalt profile shows an intensity variation that drops from 86 to 7% in a single atomic plane (Fig. 4*b*), in good agreement with the image and the predicted spatial resolution. The slight reduction in the contrast at the two planes either side of the interface is most likely due to an amorphous surface layer broadening the probe, or possibly some elastic scattering of the probe out of the channelling condition. It is important to note that for thicker specimens and for elements with higher atomic number, the effect of elastic scattering may become more pronounced.

The linescan in Fig. 4*b* clearly demonstrates atomic resolution in one dimension. As the *Z*-contrast image shows two-dimensional resolution, this result indicates that atomic resolution microanalysis from a single column is possible in principle. Col-

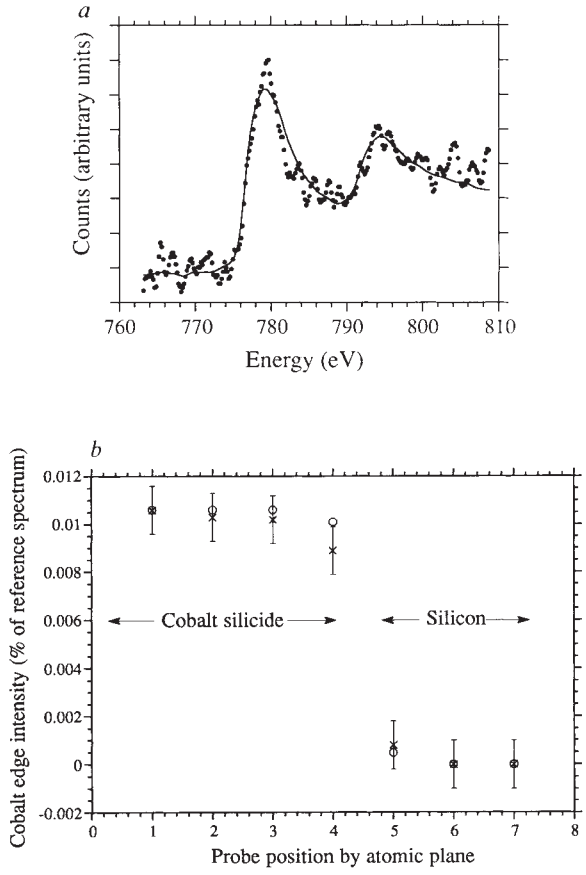

FIG. 4 *a*, The total intensity of the cobalt L-edge from planes close to the interface (●) was calculated by fitting a reference spectrum (solid line) obtained from the bulk of the silicide. The reference spectrum was again obtained by summing 20 spectra from areas of similar thickness 4–6 atomic planes from the interface, giving much improved statistics. The reference spectrum was confirmed to be characteristic of bulk $CoSi_2$ by the characteristic 2:1 $L_3:L_2$ inensity ratio[19]. The spectrum was fitted using a least-squares routine for both the pre-edge intensity to set the zero level, and also over a 30-eV window for the total cobalt intensity. (It should be noted that the co-ordination of cobalt at the interface did not appear to vary from that in the bulk, in agreement with recent interface structural models[18], though the signal-to-noise ratio is insufficient to accurately address this point.) *b*, The experimental changes (×) in the L_3 intensity (Fig. 3*b*) agree well with those expected theoretically from calculations of the probe intensity profile at the surface (○), and demonstrate clearly that atomic-resolution analysis has been achieved at the interface.

umn-by-column compositional information could be directly related to the interface structure seen in the image. This method overcomes problems caused by beam broadening and uncertainties in the interface structure that occur in microanalysis without the benefit of a high-resolution reference image[12]. At an amorphous–crystal interface of course, the usual beam broadening will occur when the probe is in the amorphous layer, but the last atomic column of the crystal can still be analysed with atomic resolution. Additionally, by increasing the number of spectra taken from each plane, it should be possible to interpret the fine structure of the spectrum in terms of the chemical bonding on the atomic scale[13], with directional information being obtained through angular deconvolution[14]. (Note that in all these situations an increase in the number of spectra is needed rather than a single longer exposure so that the effects of beam damage can be monitored.) How localized the band structure information will be from a single atomic column has yet to be determined, but a knowledge of the exact crystallographic location of the probe greatly reduces some of the ambiguities in the interpretation of spectral fine structure[15]. □

Received 14 June; accepted 30 September 1993.

1. Pennycook, S. J. & Boatner, L. A. *Nature* **336,** 565–567 (1988).
2. Pennycook, S. J. & Jesson, D. E. *Phys. Rev. Lett.* **64,** 938–941 (1990); *Acta Metall. Mater.* **40,** S149–S159 (1992).
3. Crewe, A. V., Wall, J. & Langmore, J. *Science* **168,** 1338–1340 (1970).
4. Jesson, D. E. & Pennycook, S. J. in *51st A. Proc. Microsc. Soc. Am.* (eds Bailey, G. W. & Rieder, C. L.) 978–979 (San Francisco Press, California, 1993).
5. Loane, R. F., Xu, P. & Silcox, J. *Ultramicroscopy* **40,** 121–138 (1992).
6. Browning, N. D. & Pennycook, S. J. *Microbeam Analysis* **2,** 81–89 (1993).
7. Browning, N. D., McGibbon, M. M., Chisholm, M. F. & Pennycook, S. J. in *51st A. Proc. Microsc. Soc. Am.* (eds Bailey, G. W. & Rieder, C. L.) 576–577 (San Francisco Press, California, 1993).
8. Pennycook, S. J. *Contemp. Phys.* **23,** 371–400 (1982).
9. Kohl, H. & Rose, H. *Adv. Electron. Electron Phys.* **65,** 175–200 (1985).
10. Ritchie, R. H. & Howie, A. *Phil. Mag.* A**58,** 753–767 (1988).
11. Allen, L. J. & Rossouw, C. J. *Phys. Rev.* B**42,** 11644–11654 (1990).
12. Scheinfein, M. R. & Isaacson, M. S. *J. Vac. Sci. Technol.* B**4,** 326–332 (1986).
13. Batson, P. E. *Phys. Rev.* B**44,** 5556–5561 (1991).
14. Browning, N. D., Yuan, J. & Brown, L. M. *Phil. Mag.* A**67,** 261–271 (1993).
15. Browning, N. D., Chisholm, M. F., Pennycook, S. J., Norton, D. P. & Lowndes, D. H. *Physica* C**212,** 185–190 (1993).
16. Batson, P. E. *Ultramicroscopy* **47,** 133–144 (1992).
17. de Jong, A. F. & Bulle-Lieuma, C. W. T. *Phil. Mag.* A**62,** 183–201 (1990).
18. Chisholm, M. F., Jesson, D. E., Pennycook, S. J. & Mantl, S. in *51st A. Proc. Microsc. Soc. Am.* (eds Bailey, G. W. & Rieder, C. L.) 802–803 (San Francisco Press, California, 1993).
19. De Crescenzi, M., Derrien, J., Chainet, E. & Orumchian, K. *Phys. Rev.* B**39,** 5520–5523 (1989).

ACKNOWLEDGEMENTS. We thank D. McMullan and the staff of the Microstructural Physics group at the Cavendish Laboratory for helping design, build and test the EELS system; S. Mantl for the specimen used here, and T. C. Estes, J. T. Luck and S. L. Carney for technical assistance. This research was sponsored by the US Department of Energy with Martin Marietta Energy Systems, Inc., and supported in part by an appointment to the Oak Ridge National Laboratory Postdoctoral Research Program.

Timing of the Younger Dryas event in East Africa from lake-level changes

Neil Roberts*, Maurice Taieb†, Philip Barker*, Brahim Damnati†, Michel Icole† & David Williamson†

* Department of Geography, Loughborough University of Technology, Leicester, LE11 3TU, UK
† CNRS Laboratoire de Géologie du Quaternaire, Case 907, 13288 Marseille, Cedex 9, France

THE last deglaciation was interrupted by an abrupt cooling event, the Younger Dryas, at 11,000–10,000 yr BP (uncalibrated radiocarbon timescale)[1]. Originally recognized in climate records from northwest Europe, the Younger Dryas has now been identified in marine and ice-core records worldwide[2–6]. In the tropics, a broadly contemporaneous change in climate is recorded by decreases in water levels and increased salinity of lakes[7–9,14], indicating a period of arid climate caused by a reduction in ocean-to-land moisture flux. The exact timing of these changes in relation to the Younger Dryas event in high-latitude records has remained unclear, however. Here we present climate records based on analyses of diatom assemblages, geochemistry and magnetic mineralogy of radiocarbon-dated sequences of laminated lake sediments from Lake Magadi in the East African rift. These records provide a detailed record of climate change in lowland equatorial Africa throughout the last deglaciation (12,800–10,000 ^{14}C yr BP). We find that lake-level and humidity maxima coincide with the most rapid phases of ice melting in the Northern Hemisphere, and that the climate changes, including the Younger Dryas event, were synchronous at low and high latitudes. Thus, the effects of abrupt climate change appear to be felt at both high and low latitudes without a significant time lag.

Magadi (1° 50′ S, 36° 18′ E, 600 m above sea level) is a closed lake at the southern end of the eastern (Gregory) rift (Fig. 1). It is today hypersaline-alkaline, less than 1 m deep with a trona crust, and fed almost entirely by groundwater inflows (modern springs, pH 9.0–9.5, total dissolved solids (TDS) 20–40 gl^{-1}; modern brines, pH ~ 10.5, TDS ~ 300 gl^{-1})[10,11]. Like many other East African rift lakes, Magadi contains extensive lacustrine deposits which contain evidence of significant Late Quaternary lake-level changes. These deposits include the High Magadi beds, ^{14}C dated to the early Holocene (9,120 yr BP), and marginal stromatolites with ^{14}C and U/Th dates between 12,450 and 9,650 yr BP (ref. 12). The stromatolites form a ring around both

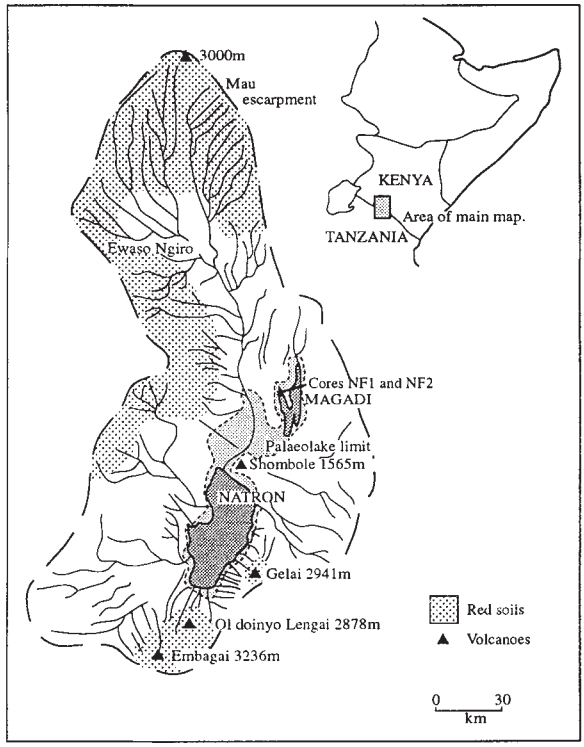

FIG. 1 Location map of the Magadi-Natron catchment, showing the extent of the modern lakes and the combined palaeolake at +60 m elevation.